

## Article

First-principles calculations of hematite ( $\alpha$ -Fe<sub>2</sub>O<sub>3</sub>) by self-consistent DFT+U+V

Nelson Naveas,<sup>1,2,3,7,\*</sup> Ruth Pulido,<sup>1,2,3</sup> Carlo Marini,<sup>4</sup> Jacobo Hernández-Montelongo,<sup>5,\*</sup> and Miguel Manso Silván<sup>1,3,6</sup>

## SUMMARY

Owing to the confined Fe-3d orbitals and self-interaction error of exchange-correlation functionals, approximate DFT fails to describe iron oxides electronic structure and magnetic properties accurately. Hybrid DFT or DFT + U can solve these problems, but the former is expensive, and the latter only considers on-site interactions. Here, we used DFT + U + V, a DFT + U extension including inter-site interactions, to simulate the structural, magnetic, and electronic properties, along with Fe and O K-edge XAS spectra of  $\alpha$ -Fe<sub>2</sub>O<sub>3</sub>. Two types of atomic orbital projectors were studied, orthogonalized and non-orthogonalized. DFT + U + V improves the description of the structural, magnetic, and electronic properties of  $\alpha$ -Fe<sub>2</sub>O<sub>3</sub> compared to approximate DFT. The accuracy of the correction depends on the orbital projector used. DFT + U + V with orthogonalized projectors achieves the best experimental agreement at a fraction of hybrid DFT cost. This work emphasizes the importance of inter-site interactions and the type of atomic orbital projectors used in the theoretical research of  $\alpha$ -Fe<sub>2</sub>O<sub>3</sub>.

## INTRODUCTION

Hematite, chemically known as  $\alpha$ -Fe<sub>2</sub>O<sub>3</sub>, has been investigated for decades because it is a relatively inexpensive and easily synthesized material, with its utility in a range of technological applications because of its low toxicity and great chemical stability.<sup>1</sup> It is used in catalysts, pollutant adsorbents, magnetic recording media, lithium-ion batteries, biomedical devices, and as a composite with different polymer matrices.<sup>1–3</sup>

Hematite is a small-band-gap semiconductor (1.9–2.6 eV)<sup>4–6</sup> with a rhombohedral crystal system and R $\bar{3}$ c space group. Two formula units are contained in each primitive unit cell ( $a_{rh} = 5.427$  Å;  $\alpha = 55.3^\circ$ ), whereas the conventional unit cell ( $a = b = 5.034$  Å;  $c = 13.75$  Å) consist of six formula units<sup>1</sup> (Figure 1). In the  $\alpha$ -Fe<sub>2</sub>O<sub>3</sub> crystal structure, a distorted octahedron of O<sup>2–</sup> ions surrounds Fe<sup>3+</sup> ions, presenting two different Fe–O distances, a shorter of 1.98 Å and a longer one of 2.09 Å. Here, the electronic configuration of Fe<sup>3+</sup> ions is  $d^5$ .

From the theoretical point of view, different methods have been utilized to study  $\alpha$ -Fe<sub>2</sub>O<sub>3</sub>.<sup>7–12</sup> In this sense, despite being the electronic structure method of choice in materials science, the approximate density functional theory (DFT)<sup>13–15</sup> faces serious challenges in accurately describing the electronic structure and magnetic properties of iron oxides.<sup>16</sup> This is because of the confined nature of the Fe-3d orbitals and the strong self-interaction error (SIE) of Local Density Approximation (LDA) or Generalized Gradient Approximation (GGA) exchange-correlation functionals.<sup>17–19</sup> The majority of the studies focused on correcting for SIE can be done with DFT + U or hybrid DFT (e.g., PBE0<sup>20</sup> and HSE06<sup>8</sup>). Hybrid DFT incorporates a fraction of Hartree-Fock exchange into standard DFT functionals.

Nevertheless, hybrid functionals are highly expensive compared to conventional DFT.<sup>21</sup> A more common choice for treating transition-metal systems is the DFT + U method,<sup>22–24</sup> which has enhanced accuracy compared to typical LDA and GGA functionals and low computational cost. In this method, an additional Coulomb repulsion term is added to the approximate DFT energy, describing the highly localized  $d$  or  $f$  electrons using the Hubbard model, whereas the remaining valence electrons are addressed using the approximated DFT functionals.<sup>25</sup> Even though the DFT + U method provides a more accurate representation of the physics in strongly correlated systems than conventional DFT, it considers just the on-site

<sup>1</sup>Departamento de Física Aplicada, Universidad Autónoma de Madrid, 28049 Madrid, Spain

<sup>2</sup>Departamento de Ingeniería Química y Procesos de Minerales, Universidad de Antofagasta, Avenida Angamos 601, Antofagasta, Chile

<sup>3</sup>Instituto Universitario de Ciencia de Materiales “Nicolás Cabrera” (INC), Universidad Autónoma de Madrid, Campus de Cantoblanco, 28049 Madrid, Spain

<sup>4</sup>CELLS–ALBA Synchrotron, 08290 Cerdanyola del Valles, Spain

<sup>5</sup>Departamento de Ciencias Matemáticas y Físicas, UC Temuco, 4813302 Temuco, Chile

<sup>6</sup>Centro de Microanálisis de Materiales, Universidad Autónoma de Madrid, Campus de Cantoblanco, 28049 Madrid, Spain

<sup>7</sup>Lead contact

\*Correspondence: nelson.naveas@estudiante.uam.es (N.N.), jacobohernandez@uct.cl (J.H.-M.)

<https://doi.org/10.1016/j.isci.2023.106033>



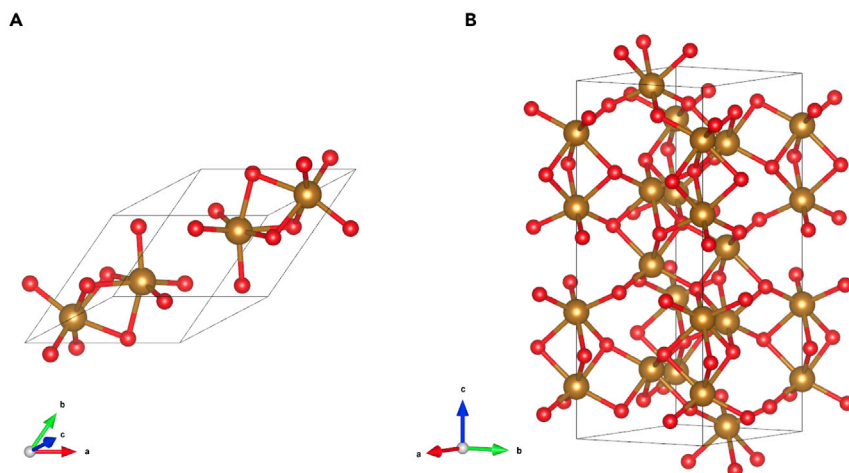


**Figure 1. Models for the crystal cell structure of the  $\alpha$ -Fe<sub>2</sub>O<sub>3</sub>**  
(A) Rhombohedral primitive cell and (B) the conventional unit cell of the  $\alpha$ -Fe<sub>2</sub>O<sub>3</sub>.

interactions. Thus, inter-site interactions between an atom and its ligands are excluded. In this context, DFT + U + V has been developed as an extension of the DFT + U method to incorporate electronic interactions both at on-site U and inter-site V levels, describing the strong inter-site electronic hybridization successfully in materials based on transition metal compounds.<sup>26,27</sup> Here, the Hubbard parameter V describes the effective interactions between electrons on nearby sites, which is important for materials that need orbital hybridization between distinct atoms. Thus, the main reason for using DFT + U + V is its greater flexibility compared to DFT + U. In particular, for systems involving transition metals (where the atomic localization of the electrons is of the d and/or f type) and surrounded by ligands. In fact, in this type of material, the electronic localization takes place in a hybridized state with constituent elements of nearby atoms. This behavior hinders the application of DFT + U because it involves only on-site localization, which can result in a distorted electronic structure for this type of material.<sup>28</sup>

Hubbard parameters were often established experimentally in the past by fitting to experimental characteristics. Furthermore, the Hubbard parameters in various materials were derived from first principles using linear-response theory (based on supercell calculations), removing the ambiguity associated with empirical determination and establishing the DFT + U + V method as an accurate and versatile approach for materials with vastly different properties.<sup>27</sup> More actually, Timrov has reworked Hubbard U linear response calculation within the context of density-functional perturbation theory (DFPT).<sup>29</sup> This approach is more computationally efficient than the previous one because it utilizes sums over monochromatic (wave-vector-specific) perturbations in primitive cells rather than finite differences between supercell computations.<sup>30</sup> In addition, it leads to increased numerical stability and convergence, as well as greater automation of the computational procedure. Recently, this formulation was expanded to include the inter-site V parameters.<sup>31</sup>

In the present study, we applied DFT + U + V to study  $\alpha$ -Fe<sub>2</sub>O<sub>3</sub> and compared it to DFT, DFT + U and PBE0 as a hybrid DFT. First, DFPT is used to compute the on-site U and V inter-site Hubbard parameters self-consistently from first-principles. Second, the converged U and V Hubbard parameters were used to optimize the structure of  $\alpha$ -Fe<sub>2</sub>O<sub>3</sub>. Then, by using DFT + U + V, we investigated the structural, magnetic, and electronic properties of  $\alpha$ -Fe<sub>2</sub>O<sub>3</sub>. Finally, to provide a deeper insight into the electronic and local structure of  $\alpha$ -Fe<sub>2</sub>O<sub>3</sub>, we carried out a theoretical and experimental study of the Fe and O K-edge by simulating the X-ray fine structure (XAFS) spectra of both uncorrected and corrected Hubbard theories.

## RESULTS AND DISCUSSION

### Hubbard parameters calculations

In the DFT + U + V method, a correction term is introduced to the approximate DFT energy functional to improve its accuracy in describing strongly correlated systems<sup>26</sup>:

$$E_{\text{DFT}+U+V} = E_{\text{DFT}} + E_{U+V} \quad (\text{Equation 1})$$

$E_{DFT}$  denotes the approximate DFT energy, whereas  $E_{U+V}$  denotes the Hubbard term, which includes both the on-site  $U$  and inter-site  $V$  Hubbard parameters. On one side, the Hubbard  $U$  parameter describes the effective strength of the on-site Coulomb repulsion. On the other side, the Hubbard parameter  $V$  describes the effective interactions between electrons on nearby sites, which is important for materials that need orbital hybridization between distinct atoms. The extended Hubbard term in the simple rotationally invariant model<sup>24</sup> is written as:

$$E_{U+V} = \frac{1}{2} \sum_l \sum_{\sigma m m'} U^l (\delta_{mm'} - n_{mm'}^{l\sigma}) n_{mm'}^{l\sigma} - \frac{1}{2} \sum_l \sum_{J(J \neq l)}^* \sum_{\sigma m m'} V^{lJ} n_{mm'}^{l\sigma} n_{m'm}^{J\sigma} \quad (\text{Equation 2})$$

Here,  $l$  and  $J$  are the atomic site indices,  $m$  and  $m'$  are the magnetic quantum numbers linked to a particular angular momentum,  $U^l$  and  $V^{lJ}$  are the effective on-site and inter-site Hubbard parameters and,  $n_{mm'}^{l\sigma}$  and  $n_{m'm}^{J\sigma}$  are the generalized occupation matrices. It is important to note that the  $*$  in the sum indicates that for each atom  $l$ , the index  $J$  encompasses all its neighbors up to a specified distance.<sup>32</sup>

In the context of our research, the on-site  $U$  correction is required for the Fe-3d states in  $\alpha$ -Fe<sub>2</sub>O<sub>3</sub>, whereas the inter-site  $V$  correction is expected to be useful in describing Fe-3d-O-2p interactions. Thus, we calculated the Hubbard parameters,  $U$  and  $V$ , for  $\alpha$ -Fe<sub>2</sub>O<sub>3</sub> using the self-consistent calculation method developed by Timrov et al., 2021<sup>31</sup> for all magnetic configurations (see Table S1 of the supplemental information). However, as shown in Figure S1 of the supplemental information, AFM-1 was demonstrated to be the most energetically favorable magnetic configuration under all studied theories, so we selected it as the ground state to compare and discuss in detail against experimental data when it is appropriated in the rest of the paper. Despite this, the main results for the other magnetic configurations (AFM-2, AFM-3, and FM) will be presented in the appropriate section of the supplemental information.

The evolution of both  $U$  and  $V$  Hubbard parameters using NAO or OAO projectors for the AFM-1 of the  $\alpha$ -Fe<sub>2</sub>O<sub>3</sub> after each iteration is shown in Figure 2. After successive iterations, the Hubbard parameters converged within 0.05 and 0.07 eV for DFT +  $U$  and DFT +  $U$  +  $V$  methods, respectively, which is enough for most post-processing applications. As shown in Figure 2, the converged values of  $U$  and  $V$  are lower than the values determined in the first iteration. Also, an enhanced variation for the  $U$  and  $V$  values using OAO than NAO projectors is found. In particular, the converged  $U$  with OAO projectors is roughly 1 eV lower than its initial value in the DFT +  $U$  +  $V$  approach. Hubbard  $V$  for the two different combinations of Fe and O atoms found in  $\alpha$ -Fe<sub>2</sub>O<sub>3</sub> exhibits a similar convergence tendency. Moreover, Hubbard  $V$  has a significantly smaller variation of their initial value (0.2–0.6 eV). Such as previously reported for SrTiO<sub>3</sub><sup>27</sup> and MnPO<sub>4</sub>, and LiMnPO<sub>4</sub><sup>31</sup>, the structural optimization contained in the self-consistent approach is critical for obtaining the final values of the Hubbard parameters.

As a result of the sensitivity of the Hubbard atoms to their surrounding chemical environment,<sup>33</sup> surely boosts the change of  $U$  and  $V$  during the self-consistent cycle.<sup>31</sup> The converged self-consistent Hubbard parameters  $U$  and  $V$  for the AFM-1 of the  $\alpha$ -Fe<sub>2</sub>O<sub>3</sub> are summarized in Table 1. The following section will use these values to discuss the structural properties of  $\alpha$ -Fe<sub>2</sub>O<sub>3</sub> (AFM-1) and evaluate the magnetic and electronic properties.

## Structural properties

After calculating the Hubbard parameters, we compare the structural properties of the conventional unit cell of  $\alpha$ -Fe<sub>2</sub>O<sub>3</sub> optimized at the three levels of theory used in this study (DFT, DFT +  $U$ , and DFT +  $U$  +  $V$ ). Table 2 shows the optimized lattice parameters ( $a$  and  $c$ ), as well as the equilibrium volume ( $V$ ) of the conventional unit cell for the AFM-1 of the  $\alpha$ -Fe<sub>2</sub>O<sub>3</sub> compared to the experimental values. The experimental lattice parameters of the  $\alpha$ -Fe<sub>2</sub>O<sub>3</sub> have been obtained from the entry # 9015964<sup>11</sup> from the Crystallography Open Database (COD). Alternatively, the optimized lattice parameters for the AFM-2, AFM-3 and FM configurations are presented in Table S2 of the supplemental information. As previously reported for  $\alpha$ -Fe<sub>2</sub>O<sub>3</sub>,<sup>34</sup> the standard DFT method underestimates the lattice parameters ( $\Delta a \approx -2.44\%$  and  $\Delta c \approx -1.01\%$ ) and volume ( $\Delta V \approx -6.01\%$ ). On the contrary, both Hubbard-corrected DFT methods (DFT +  $U$  and DFT +  $U$  +  $V$ ) significantly improve the fitting with the experimental lattice parameters and volume. Depending on the used Hubbard-corrected method, the difference between the calculated and experimental values decreases to 0.4–0.6% for  $a$ , 0.2–0.49% for  $c$ , and 0.72–1.37% for  $V$ . This improving in the description of the structural properties of  $\alpha$ -Fe<sub>2</sub>O<sub>3</sub> has been widely reported for DFT +  $U$  approach (including only the on-site type of correction).<sup>7,34</sup> In addition, it is essential to note that the Hubbard projector type substantially impacts the DFT results obtained with DFT +  $U$  and DFT +  $U$  +  $V$ . In

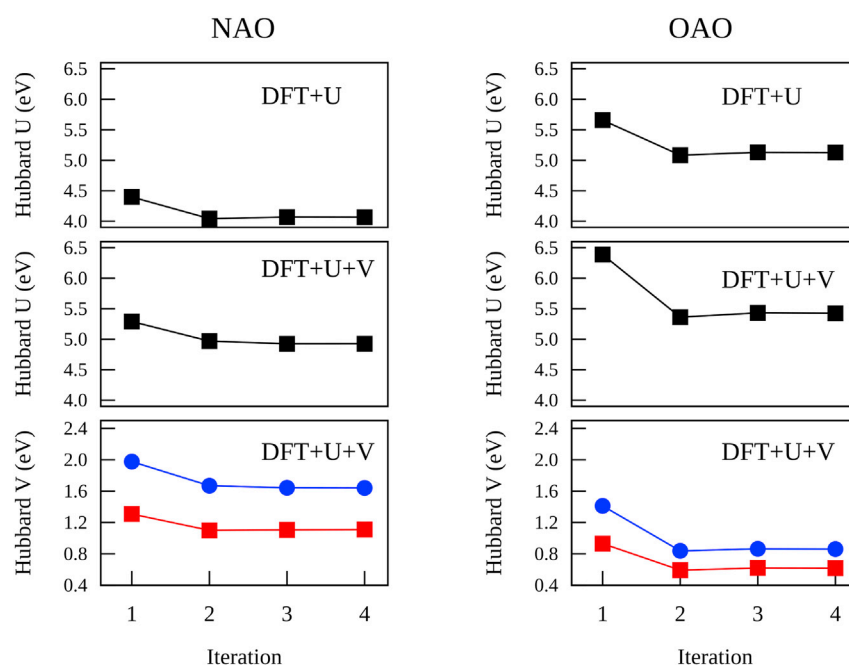


**Figure 2. Evolution of U and V Hubbard parameters using NAO or OAO projectors for the AFM-1 configuration of  $\alpha$ -Fe<sub>2</sub>O<sub>3</sub> after each iteration of the self-consistent calculations based on DFT + U and DFT + U + V**

The blue and red lines in the Hubbard V curves correspond to the Hubbard V parameters related to the shorter and longer Fe-O distances.

particular, as shown in Table 2, we find that when using NAO projectors, DFT + U slightly overestimates the lattice parameters ( $\Delta a \approx 0.5\%$  and  $\Delta c \approx 0.37\%$ ) and the equilibrium volume ( $\Delta V \approx 1.37\%$ ). On the other hand, DFT + U + V underestimates the lattice parameter a, whereas it overestimates the lattice parameters c and volume, although it has a better agreement with the experimental one compared to the standard DFT. Then, it is found that the best agreement with experiments is obtained at the DFT + U level in the case of NAO projectors.

As OAO projectors are used, DFT + U and DFT + U + V slightly overestimate the lattice parameters and volume. However, these structural properties are more precisely described by DFT + U + V when using OAO projectors. As a result, we may conclude that when OAO projectors are employed, DFT + U + V is more consistent with the experimental values than DFT + U alone. On the contrary, it is found that in the case of NAO projectors, the best agreement with experiments is obtained at the DFT + U level. In this way, no one scenario agrees with experiments the best when the lattice parameters and volume are both considered concurrently; however, the most accurate findings are obtained using DFT + U + V(OAO).

In the hematite structure, the anions ( $O^{2-}$ ) are organized in a hexagonal closed-packed lattice (hcp) with the cations ( $Fe^{3+}$ ). Two-thirds of the sites are occupied by  $Fe^{3+}$  ions, which are grouped in a regular pattern, with two occupied sites followed by one unoccupied site on the (001) plane, generating 6-fold rings.<sup>1,37</sup>

**Table 1. Converged Hubbard parameters for the crystal cell of  $\alpha$ -Fe<sub>2</sub>O<sub>3</sub> (AFM-1 configuration) calculated from first principles using DFPT**

Method	Hubbard manifolds	Hubbard Parameter (eV)	
DFT + U	NAO	U	4.062
	OAO	U	5.126
DFT + U + V	NAO	U	4.926
		V	1.641/1.110
	OAO	U	5.425
		V	0.861/0.618

**Table 2. Optimized structural parameters of the conventional unit cell for the AFM-1 configuration of the  $\alpha$ -Fe<sub>2</sub>O<sub>3</sub> calculated by DFT, DFT + U, and DFT + U + V theories and their comparison with results obtained from previous studies**

Hubbard manifold	Method	a = b (Å)	c (Å)	c/a	V(Å <sup>3</sup> )	Reference
–	Experimental	5.034	13.75	2.73	301.771	Finger and Hazen <sup>11</sup>
–	DFT	5.003	13.870	2.78	347.17	Rollmann et al. <sup>35</sup>
Not specified	DFT + U	5.026	13.750	2.74	347.33	Rollmann et al. <sup>35</sup>
–	DFT	5.007	13.829	2.78	346.70	Rohrbach et al. <sup>34</sup>
Not specified	DFT + U	5.067	13.882	2.74	356.41	Rohrbach et al. <sup>34</sup>
Not specified	DFT + U	5.07	13.88	2.74	356.78	Adelstein et al. <sup>36</sup>
–	DFT	4.914	13.612	2.77	284.650	This study
NAO	DFT + U	5.059	13.801	2.73	305.950	This study
	DFT + U + V	5.004	13.817	2.76	299.603	
OAO	DFT + U	5.064	13.778	2.72	305.951	This study
	DFT + U + V	5.055	13.793	2.73	305.204	

The experimental lattice parameters have been obtained from the COD entry # 9015964.<sup>11</sup>

The arrangement of the cations results in pairs of FeO<sub>6</sub> octahedra that share edges with three adjacent octahedra in the same plane and have one face in an adjacent plane in the [001] direction.<sup>38</sup> Octahedral face sharing along the c-axis is what causes the cation sub-lattice to deviate from ideal packing; Fe atoms in shared octahedra are repelled in the direction normal to [001], causing the cations to shift closer to the unshared faces.<sup>39</sup> It results in three of the Fe-O bonds having a shorter bond length. Then, we analyzed the Fe-Fe interatomic distance and Fe-O bond lengths. The optimized and experimental values of the Fe-Fe interatomic distance and Fe-O bond lengths for the AFM-1 configuration of the  $\alpha$ -Fe<sub>2</sub>O<sub>3</sub> are illustrated in Figure 3. In the conventional unit cell of  $\alpha$ -Fe<sub>2</sub>O<sub>3</sub>, there are both two types of Fe-Fe interatomic distances (2.88 Å and 3.98 Å, Figure 3A) and Fe-O bond lengths (1.9 Å and 2.06 Å, Figure 3B) observed experimentally.<sup>40</sup> As shown in Figure 3A, DFT + U + V(OAO), DFT + U(OAO), and DFT + U(NAO) provide the best agreement for the Fe-Fe interatomic distance with the experimental reported value. DFT + U + V(NAO) method slightly overestimates the Fe-Fe interatomic distance. In the case of the Fe-O bond lengths, although the difference between these two values is small, it still possible to resolve them precisely in calculations. Again, DFT + U + V(OAO), DFT + U(OAO) and DFT + U(NAO) provide the best agreement for the Fe-O bond lengths with these two experimental distances (Figure 3B).

### Magnetic properties

The magnetic properties of  $\alpha$ -Fe<sub>2</sub>O<sub>3</sub> are strongly influenced by the temperature and the particle size.<sup>41</sup>  $\alpha$ -Fe<sub>2</sub>O<sub>3</sub> is slightly ferromagnetic at room temperature but becomes paramagnetic at 956 K (*T<sub>d</sub>*). At 263 K, it experiences a magnetic phase transition from magnetic to antiferromagnetic. This lower temperature transition is referred to as the Morin temperature (*T<sub>M</sub>*), below which the two magnetic sub-lattices are perfectly antiparallel and aligned along the rhombohedral [111] axis. In our study, we take into account the AFM-1 spin configuration (++–), which is known to be the more energetically stable (see Figure S1). Figure 4 shows the magnetic moments on Fe atoms in  $\alpha$ -Fe<sub>2</sub>O<sub>3</sub>. Likewise, the magnetic moments for the AFM-2, AFM-3 and FM configurations are shown in Table S3 of the supplemental information. The experimental value of the magnetic moment for  $\alpha$ -Fe<sub>2</sub>O<sub>3</sub> has been reported between 4.0 and 4.6  $\mu_B$ /Fe atom.<sup>10,42,43</sup> The magnetic moment calculated by DFT was about 0.9–1.5  $\mu_B$ /Fe atom lower than the experimental value. Although the Hubbard corrections underestimate the magnetic moment, it improves the estimation for all situations. The closest agreement with the experimental value on average is obtained when using DFT + U and OAO (0.1–0.7  $\mu_B$ /Fe atom lower than the experimental value). In contrast, the most significant underestimation from the experimental value on average is obtained when using DFT + U + V and NAO (0.4–1.0  $\mu_B$ /Fe atom lower than the experimental value).

### Electronic properties

Various experimental techniques have been used to examine the electronic structure of  $\alpha$ -Fe<sub>2</sub>O<sub>3</sub>. A substantial hybridization between O-2p and Fe-3d levels has been shown in the valence band, whereas Fe-3d states dominate the conduction band of  $\alpha$ -Fe<sub>2</sub>O<sub>3</sub>.<sup>44–46</sup> Thus,  $\alpha$ -Fe<sub>2</sub>O<sub>3</sub> has been classified as a charge-transfer or intermediate insulator.<sup>44</sup> The band structure and projected density of state (PDOS)

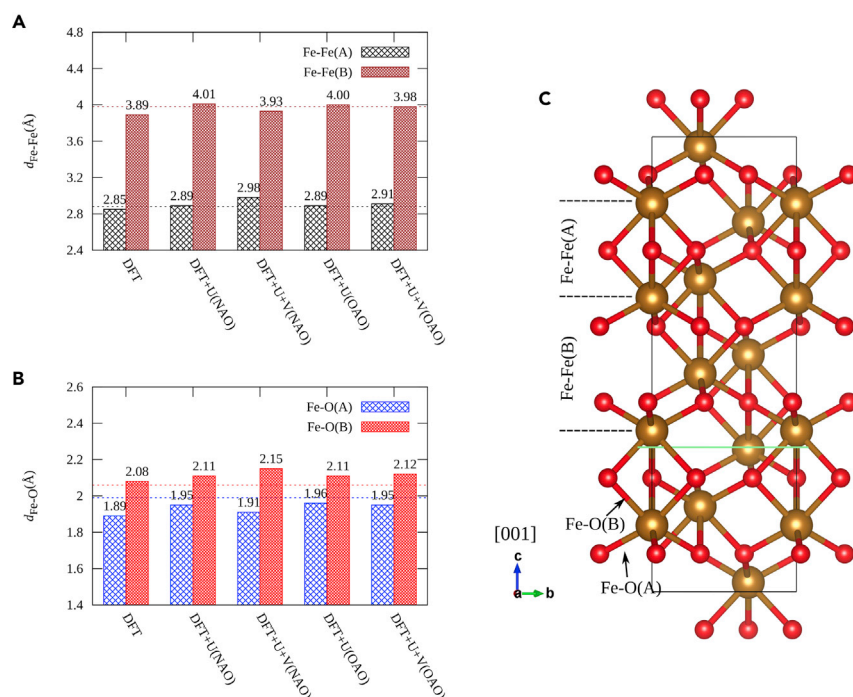


**Figure 3. Optimized interatomic distances in the crystal cell of  $\alpha$ -Fe<sub>2</sub>O<sub>3</sub> (AFM-1 configuration) calculated by DFT, DFT + U, and DFT + U + V theories**

(A) Fe-Fe interatomic distances, (B) Fe-O bond lengths and (C) their schematic representation in the  $\alpha$ -Fe<sub>2</sub>O<sub>3</sub> conventional unit cell. Dash lines correspond to the experimental values.<sup>40</sup>

for the AFM-1 of the  $\alpha$ -Fe<sub>2</sub>O<sub>3</sub> by using standard DFT are shown in Figure 5. As shown in the band structure of Figure 5, there is a huge discrepancy between DFT estimates and the actual reported experimental band gap value. DFT underestimates the band gap, resulting in a value of 0.2 eV compared to the experimental band gap value of 2.6 eV reported by Zimmermann.<sup>6</sup> The pDOS and total DOS at the DFT level show that the conduction bands minimum in the DFT situation is predominantly Fe-3d, whereas the valence bands maximum is mixed, exhibiting a substantial hybridization between the Fe-3d and O-2p states. Overall, because of high hybridization with O-2p states, Fe-3d states are over-delocalized owing to SIE inherent to the standard DFT.

Figure 6 shows the total DOS and pDOS calculated for the AFM-1 of the  $\alpha$ -Fe<sub>2</sub>O<sub>3</sub> by comparing the standard DFT used in this study (PBEsol) against the PBE0 hybrid DFT functional. Here, the PBE0 exchange functional is tested with different exchange fractions. Also, it is important to note that the DOS and pDOS for the PBE0 functional were obtained by doing an SCF calculation on the previously obtained DFT-PBEsol optimized structure. On the one hand, PBE0 at 25% of the exchange fraction largely overestimates the band gap, resulting in a value of 4.23 eV. On the other hand, PBE0 at 14% of the exchange fraction results in an excellent agreement with the experimental band gap value of 2.6 eV.

Moreover, the use of PBE0 improves the localization of the Fe states. However, despite showing an excellent result, the utilization of hybrid functionals, such as PBE0, is significantly more expensive than DFT and Hubbard-corrected DFT methods.<sup>21</sup> Indeed, under our hardware and configuration system, an SCF PBE0 calculation takes approximately 70 times more CPU time than the DFT + U + V(OAO) calculation. Another disadvantage of hybrid calculations is that they are not totally computed from first-principles. In fact, the exchange fraction in a hybrid calculation is known to be a material-dependent quantity typically calculated by fitting experimental data. In contrast, the DFT + U + V approach relies on Hubbard U and V parameters that are simultaneously computed from first principles and with a self-consistent procedure, not relying on any empirical parameters.<sup>27</sup>

Figure 7 shows the band structure and pDOS for the AFM-1 of the  $\alpha$ -Fe<sub>2</sub>O<sub>3</sub> by using Hubbard-corrected approaches. In addition, the pDOS for the AFM-2, AFM-3 and FM configurations are presented in

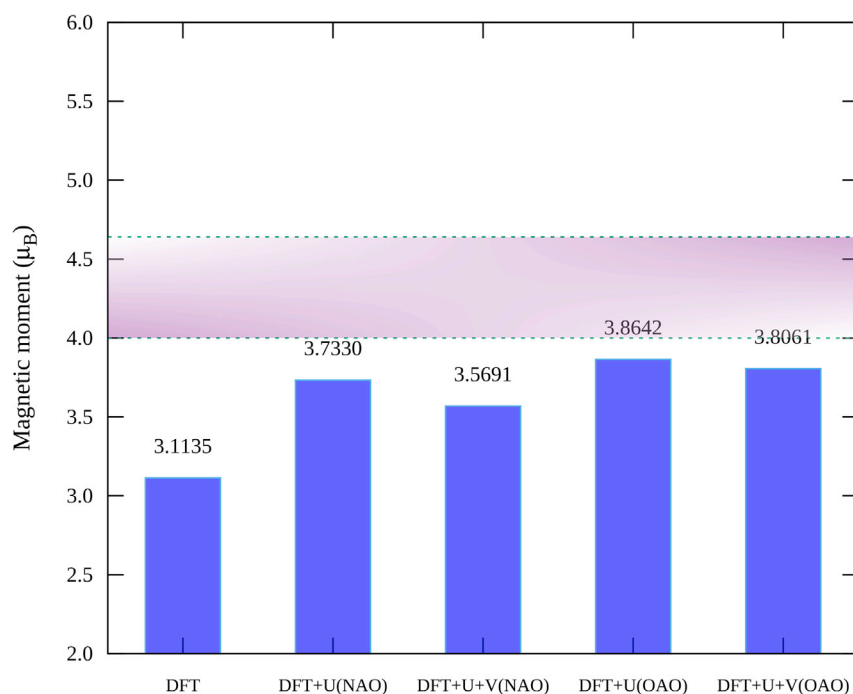


**Figure 4. Magnetic moment of Fe in the unit crystal cell for the AFM-1 of the  $\alpha$ -Fe<sub>2</sub>O<sub>3</sub> calculated by DFT, DFT + U, and DFT + U + V theories**

The zone between dashed lines corresponds to the range of the experimental magnetic moment values between 4.0–4.6  $\mu_B/\text{Fe atom}$ .<sup>10,42,43</sup>

Figures S2–S4, respectively, of the supplemental information. In general, we found that  $\alpha$ -Fe<sub>2</sub>O<sub>3</sub> has both a direct and indirect gap, which is consistent with previous theoretical investigations.<sup>8</sup> Of interest, compared to standard DFT, Hubbard corrections increase the band gap value to 1.6–2.5 eV, depending on the method and the used Hubbard projector type. On the one hand, the AFM-1 configuration showed that at the DFT + U level, NAO strongly underestimates the band gap value (1.6 eV) compared to OAO (2.18 eV). On the other hand, DFT + U + V improves the band gap estimation using NAO (2.18 eV) and OAO (2.48 eV) projectors. Conversely, the pDOS and total DOS at the DFT + U and DFT + U + V levels show the on-site Hubbard U correction for the Fe-3d states and the inter-site Hubbard V correction for the Fe-3d and O-2p states can be used to correct SIE. As seen in Figures 7A and 7B, applying the Hubbard U correction to Fe-3d states renders them significantly more localized than in standard DFT. The spectral weight of occupied Fe-3d states is moved to lower energies with slight variations depending on the Hubbard correction type. The empty Fe-3d states are shifted to higher energies and have a higher intensity, which is a sign of enhanced localization. The top of the valence bands clearly has an O-2p character, whereas the lowest conduction bands have a strong mixed character, highlighting the Fe-3d-O-2p hybridization. The Fe-3d character dominates the higher energy empty states, with peaks ranging from 2 to 4 eV depending on the Hubbard correction.

### Fe and O K-edge spectra simulation

X-ray absorption fine structure (XAFS) spectroscopy is a very powerful element-specific technique that provides both electronic and local probes. In general, the XAFS signal may be divided into two regions: near-edge (XANES: X-ray absorption near-edge structure) and extended (EXAFS: extended X-ray absorption fine structure). Each region includes information that is distinct and complementary. The XANES area begins with the absorption signal being elevated and extends up to 100–150 eV above the edge. The XANES characteristics are derived from the details of the density of empty states at the Fermi level and huge multiple scattering processes; hence, the XANES area contains information about the electronic properties and local geometry around the absorber. The fine structure in the EXAFS region is primarily owing to single scattering events, which yields a relatively simple formula (standard EXAFS formula) that is easily



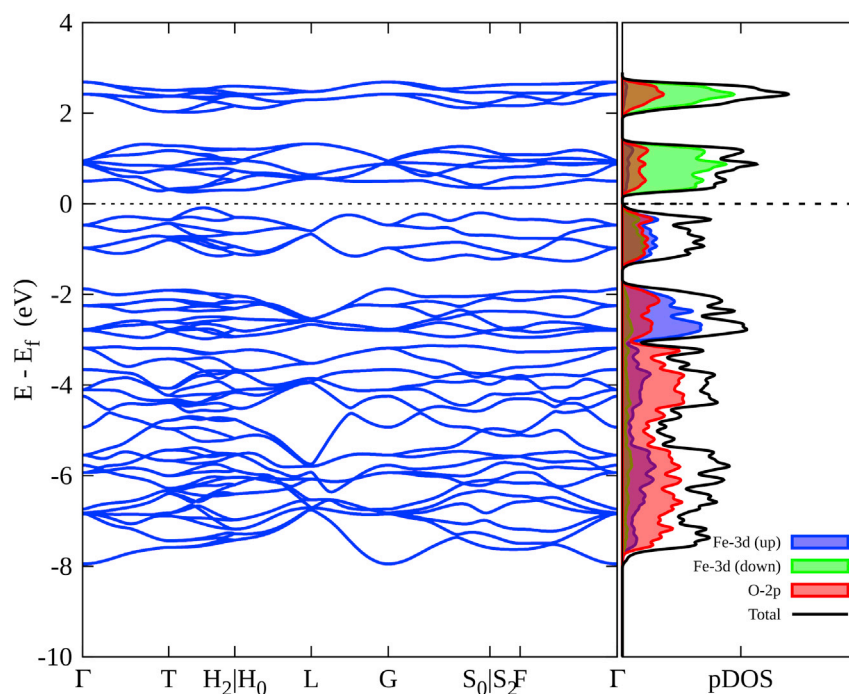


**Figure 5. Band structure and partial density of states (pDOS) for the AFM-1 of the  $\alpha$ -Fe<sub>2</sub>O<sub>3</sub> bulk crystal calculated by standard DFT**

interpretable in terms of local structure parameters: coordination numbers, distances, and disorder of neighboring shells.<sup>47</sup>

For the reasons discussed above, we obtained the experimental and calculated Fe and O K-edge XANES spectra of the  $\alpha$ -Fe<sub>2</sub>O<sub>3</sub> by using both uncorrected and corrected Hubbard approaches (Figure 8). Herein, we used the conventional unit cell of the AFM-1 spin configuration again because it is more stable energetically (see Figure S1). Figure 8A compares the experimental Fe K-edge XANES spectra of the  $\alpha$ -Fe<sub>2</sub>O<sub>3</sub> and the simulated ones by the different theories used in this study. First, it is essential to mention that previously reported observations<sup>48,49</sup> and our present experimental spectrum are in excellent agreement. Secondly, in general, the shape of simulated spectra is quite similar to the experimental one. Remarkably, standard DFT theory results in a quite well spectrum. However, major differences appear in the pre-edge region. The simulated spectra present a displacement toward higher energy.

On the other hand, the application of Hubbard corrections to both DFT + U and DFT + U + V results in important changes in the spectra, mainly located in the pre-edge region. There is an additional shift toward higher energy in the peak position, and one of the pre-edge peaks is loose. This likely happens because of the highly localized states. According to previous research, the K pre-edge characteristics are attributed to electronic transitions of quadrupole nature between 1s and 3d orbitals and/or to the dipole transition between 1s and 4p hybridized with 3d orbitals.<sup>50,51</sup> Two quadrupole transitions for octahedral compounds with centrosymmetric sites are predicted theoretically: 1s-3d (*t*<sub>2g</sub>) and 1s-3d (*e*<sub>g</sub>). However, experimentally one to three more components are readily visible in hematite.<sup>51,52</sup>

In oxygen K-edge X-ray absorption, an X-ray with 530 eV energy excites the initial state of the system to a final state. The simulations of the O 1s K-edge XANES of  $\alpha$ -Fe<sub>2</sub>O<sub>3</sub> are shown in Figure 8B. The simulations are compared to the experimental O 1s K-edge XANES of  $\alpha$ -Fe<sub>2</sub>O<sub>3</sub> reported by Wu et al., 1997.<sup>53</sup> The experimental spectra of Ferrites (Fe<sub>2</sub>O<sub>3</sub>) have a 3d5 ground state and may be found in various crystal forms, with the  $\alpha$ -Fe<sub>2</sub>O<sub>3</sub> structure being the most prevalent.<sup>53,54</sup> Characteristic splits between 530.8 and 532.2 eV related to the spin-down *t*<sub>2g</sub> and *e*<sub>g</sub> states are observed. Remarkably, the simulated results by DFT theory confirmed a close agreement with those obtained from experimental spectra. In the pre-edge region, the expected outcome of splitting is presented. In contrast, the splitting related to *t*<sub>2g</sub>-*e*<sub>g</sub> symmetry bands



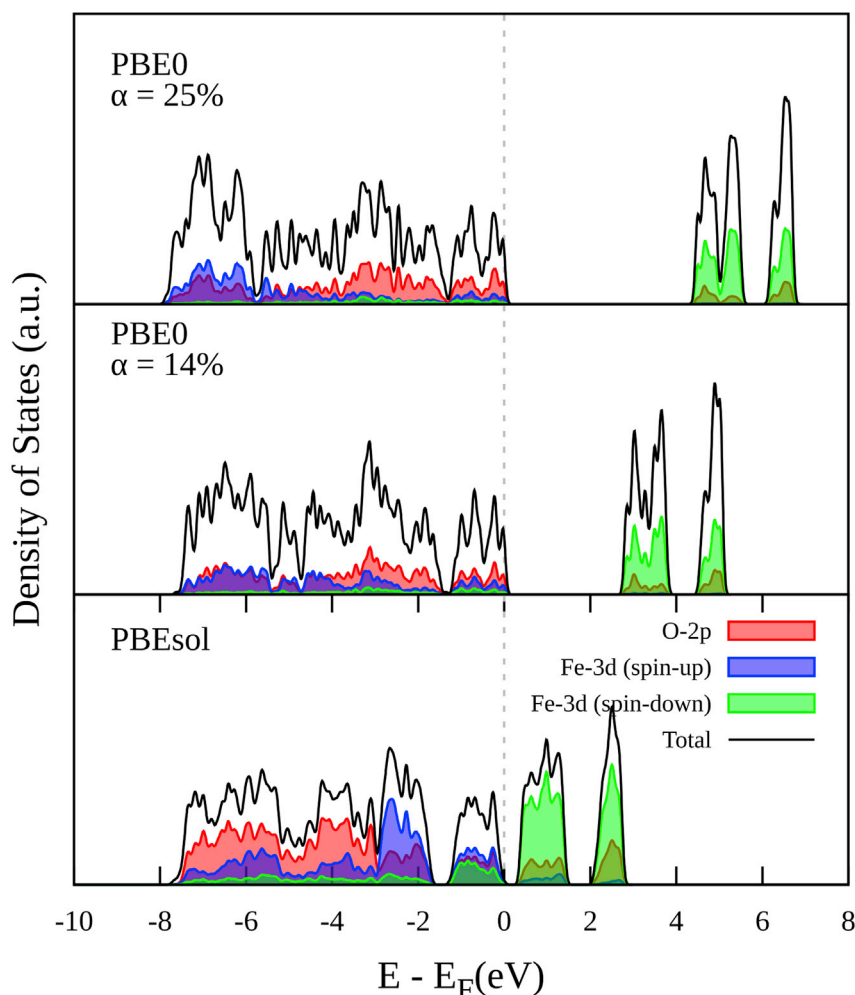


**Figure 6.** Partial density of states (pDOS) for the AFM-1 of the  $\alpha$ -Fe<sub>2</sub>O<sub>3</sub> bulk crystal calculated by DFT and the hybrid functional PBE0

expected in the pre-edge region is lost when the Hubbard corrections of both DFT + U and DFT + U + V are applied. To further explore these results, we compare the experimental and calculated O K-edge XANES of  $\alpha$ -Fe<sub>2</sub>O<sub>3</sub> with the unoccupied states of the pDOS for the AFM-1 configuration (Figure S5 of the supplemental information). More specifically, the first two peaks in XANES from DFT originate from the hybridization with Fe-3d minority spin states. The position of the two peaks is 1.25 eV and 2.55 eV, whereas the experimental ones are found at 2.25 and 3.78 eV, respectively. Also, the splitting between these two peaks is in fairly good agreement with the experiments (1.30 eV and 1.53 eV). The application of the Hubbard U correction to Fe-3d states significantly alters the XANES spectrum, because of the blueshift in the energy of the Fe-3d states. The Hubbard correction does not improve in every aspect of the results, because now the splitting between the  $t_{2g}$  and  $e_g$  states is much smaller than in DFT, and consequently the distance in energy between the two peaks drastically reduces, leading to these two features to merge (Figure S5). However, the change in the Fe-3d density of state produces a better agreement in the energy position concerning the simple DFT case. In this regard, we can conclude that the Hubbard corrections do not improve in every aspect of the XANES spectra of  $\alpha$ -Fe<sub>2</sub>O<sub>3</sub>, and maybe a different theory is necessary to explain these spectra better.

Finally, we tested the validity of each model by checking the likelihood of the obtained structures with respect to the experimental EXAFS data at the Fe K edge. A quantitative comparison is thus achieved considering the statistical meaning of each fit in terms of  $\chi^2$ . The experimental data and best-fit curves by EXAFS signal are shown in Figure 9 and Table S4 of the supplemental information. In all the cases,

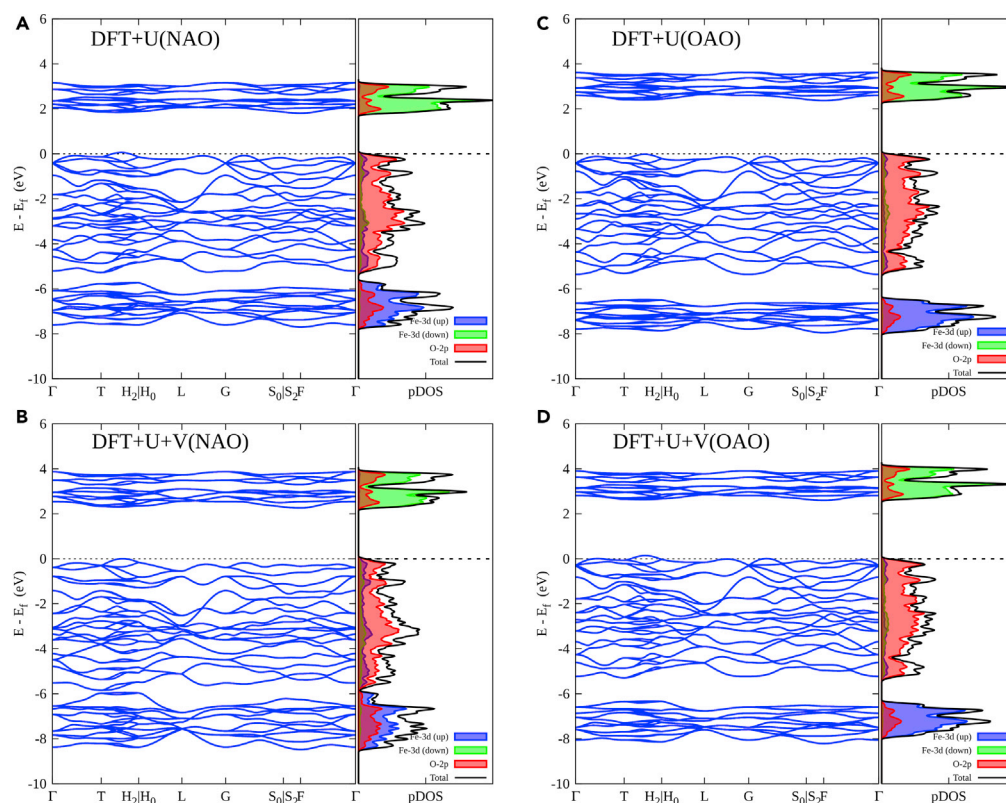


**Figure 7. Band structures and partial density of states (pDOS) for the AFM-1 of the  $\alpha$ -Fe<sub>2</sub>O<sub>3</sub> bulk crystal calculated by DFT, DFT + U and DFT + U + V**

- (A) DFT + U using NAO projectors.  
(B) DFT + U using OAO projectors.  
(C) DFT + U + V using NAO projectors.  
(D) DFT + U + V using OAO projectors.

the same number of parameters has been adopted: the first peak located around 1–2 Å (which mimics the Fe-O octahedra) has been modeled by two distances of Fe-O and a unique Debye-Waller factor (i.e., one order parameter), whereas the doublet around 2 and 4 Å (which mimics Fe-Fe interactions) contains three paths corresponding to 3 distance and 2 Debye-Waller factors. The total amplitude parameter was fixed to 0.85 for all the models (after preliminary adjustment on Fe foil), whereas correction to the energy scale has been set free to vary. In general, the results of simulations were in close agreement with experimental spectrum data. Of interest, from a statistical point of view, a discrepancy between observed values and the values expected under the model used was evidenced (see [Figure S6](#) and [Table S5](#) of the [supplemental information](#)). The best-simulated curve adjustment to the experimental data was by DFT + U (NAO and OAO projectors) method, while on the contrary, DFT + U + V(NAO) presented the worst adjustment to the experimental data. Although DFT + U + V(OAO) does not result in the best curve adjustment, the difference between this theory and DFT + U theories is only marginal, which suggests that DFT + U + V(OAO) theory is also a good choice for simulating XAFS spectra.

## Conclusion

In this work, the structural, magnetic, and electronic characteristics of  $\alpha$ -Fe<sub>2</sub>O<sub>3</sub> have been investigated by a fully first-principles approach. By using the DFT + U + V method with on-site U and inter-site V Hubbard parameters derived from DFPT, we have compared the results against DFT, DFT + U, and PBE0 as a hybrid functional. In addition, two types of Hubbard projectors based on NAO and OAO projectors have been used. First, based on the orientation of the local spin density around the Fe atoms of  $\alpha$ -Fe<sub>2</sub>O<sub>3</sub>, we found that the AFM-1 (+ + -) is the most energetically favorable magnetic configuration under all studied theories. More interestingly, we discovered that the expected outcomes vary significantly depending on whether only U or both U and V corrections are used, as well as the Hubbard projector type. The best overall

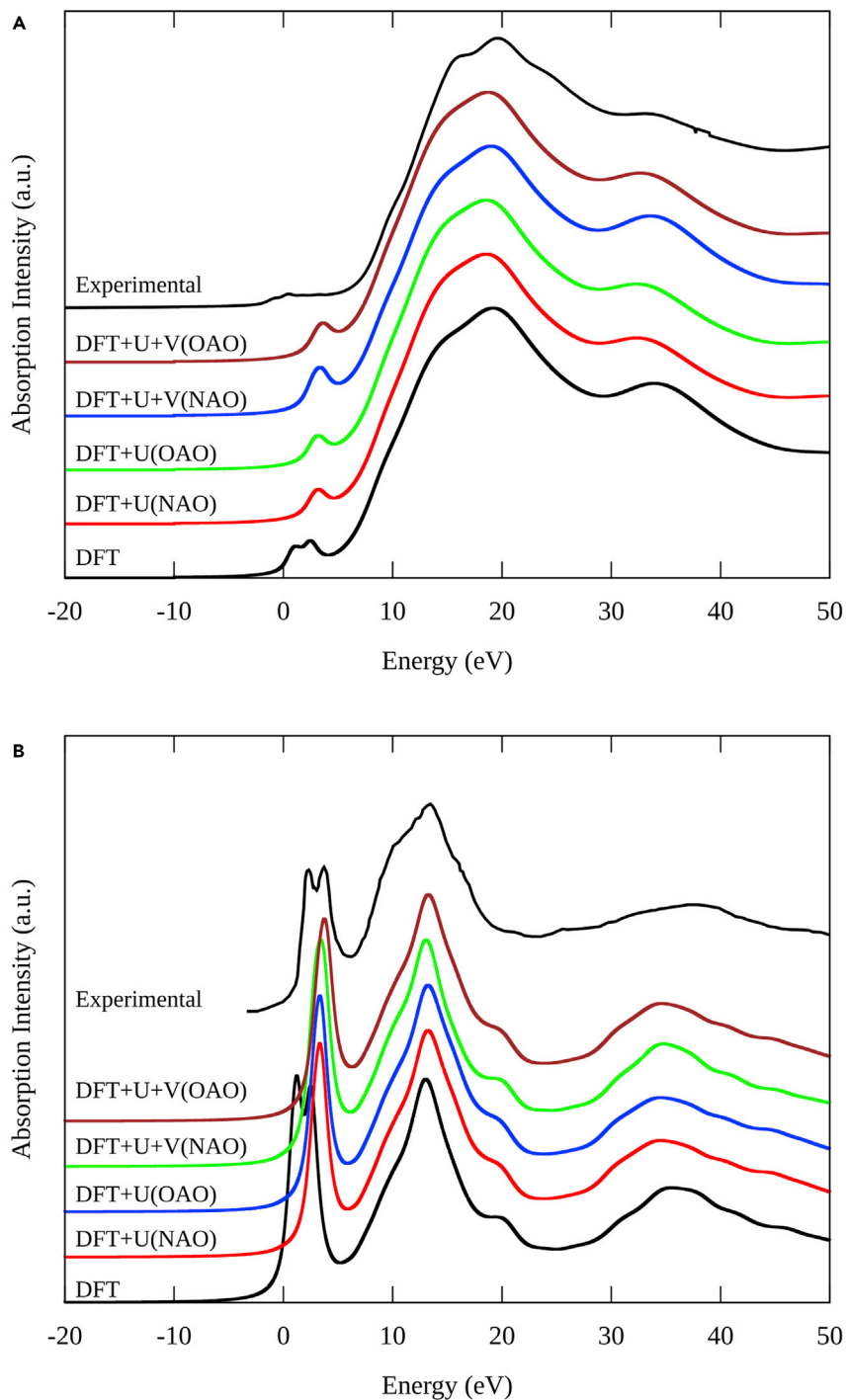


**Figure 8. Experimental and simulated Fe and O K-edge XANES the  $\alpha$ -Fe<sub>2</sub>O<sub>3</sub> bulk crystal (AFM-1 configuration) calculated by DFT, DFT + U and DFT + U + V**

(A) Fe K-edge and O (B) K-edge XANES of the  $\alpha$ -Fe<sub>2</sub>O<sub>3</sub> bulk crystal (AFM-1 configuration) calculated by the different theories.

agreement is found when using DFT + U + V with OAO projectors. Here, the on-site U parameter is important for describing the confined nature of Fe-3d states, whereas the inter-site V parameter is relevant for describing the strong hybridization between Fe-3d and O-2p states. The extended Hubbard functional

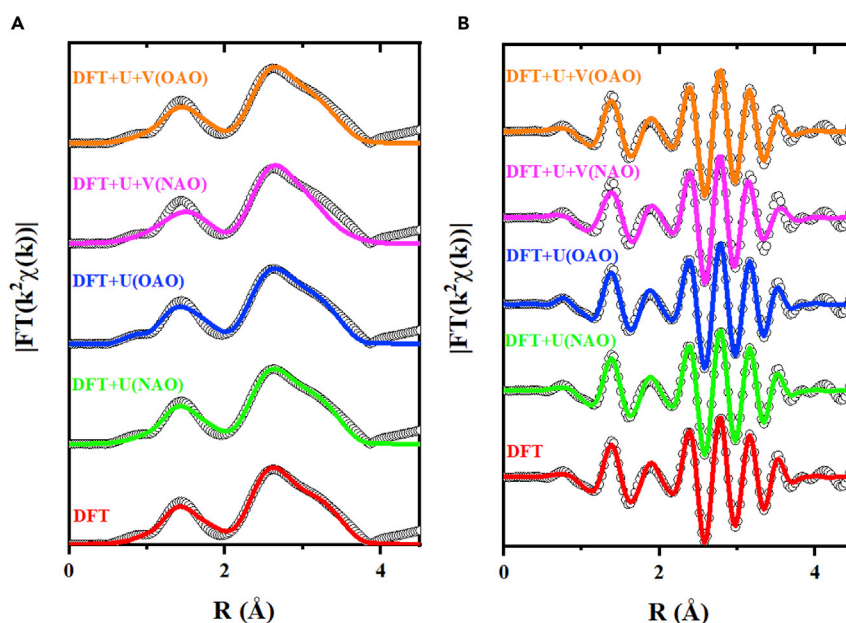


**Figure 9. The Fourier Transformed (FT) of the experimental and simulated Fe K-edge EXAFS for the AFM-1 of the  $\alpha$ -Fe<sub>2</sub>O<sub>3</sub> bulk crystal**

(A) Real and (B) imaginary part of fits (lines) of the FT signal from  $k^2$ -weighted EXAFS signals (dots) calculated by DFT, DFT + U, and DFT + U + V theories.

improved the description of the structural, magnetic, and electronic properties of  $\alpha$ -Fe<sub>2</sub>O<sub>3</sub> compared to standard DFT.

Moreover, compared to hybrid functional, DFT + U + V gives a similar picture without excessive computing resources. We are confident that DFT + U + V with OAO projectors can be critical in improving spectra simulation in materials science, particularly for  $\alpha$ -Fe<sub>2</sub>O<sub>3</sub>. Thus, this work highlights the importance of taking into account the inter-site interactions as well as the necessity to consider the type of atomic orbital projectors to use in future theoretical research of  $\alpha$ -Fe<sub>2</sub>O<sub>3</sub>. The present study also suggests the need for the inter-site V parameter for other binary oxide systems, which involve transition metals and hybridized electronic states with constituent elements of nearby atoms. Nevertheless, we emphasize the need for ongoing research to unclear the extension of DFT + U + V to other binary oxides. Similarly, another significant challenge for future research will be determining the potential impact of the DFT + U + V theory on the surface engineering of  $\alpha$ -Fe<sub>2</sub>O<sub>3</sub> and other systems. Thus, promising opportunities are open for DFT + U + V theory in computational materials science.

## STAR★METHODS

Detailed methods are provided in the online version of this paper and include the following:

- KEY RESOURCES TABLE
- RESOURCE AVAILABILITY
  - Lead contact
  - Materials availability
  - Data and code availability
- EXPERIMENTAL MODEL AND SUBJECT DETAILS
- METHOD DETAILS
- QUANTIFICATION AND STATISTICAL ANALYSIS
- ADDITIONAL RESOURCES

## SUPPLEMENTAL INFORMATION

Supplemental information can be found online at <https://doi.org/10.1016/j.isci.2023.106033>.

## ACKNOWLEDGMENTS

We recognize to PhD. Programs in “Advanced Materials and Nanotechnologies” from Universidad Autónoma de Madrid (UAM, Spain) and “Ingeniería de Procesos de Minerales” from Universidad de Antofagasta (UA, Chile). This work was financially supported by CONICYT PFCHA/DOCTORADO/2017-21172001 (Nelson Naveas) and partially funded by project USAMPESA, PID-2020-112770-C22, from the Government of Spain. Moreover, we acknowledge ALBA synchrotron facility for beamtime no. 2020024325 at the CLÆSS beamline. The simulations used in this paper have been performed in the Centro de Computación Científica-Universidad Autónoma de Madrid (CCC-UAM); thanks to CPU time and other resources granted by the institution.

## AUTHOR CONTRIBUTIONS

Conceptualization, N.N. and M.M.S.; theoretical calculations, N.N. and R.P.; experimental analysis, N.N. and C.M.; computational simulations, N.N., J.H-M., and M.M.S.; writing—original draft preparation, N.N. and R.P. All authors have read and agreed to the published version of the manuscript.

## DECLARATION OF INTERESTS

The authors declare no conflict of interest. The funders had no role in the design of the study; in the collection, analyses, or interpretation of data; in the writing of the manuscript; or in the decision to publish the results.

Received: July 14, 2022

Revised: September 22, 2022

Accepted: January 18, 2023

Published: January 24, 2023

## REFERENCES

1. Tamirat, A.G., Rick, J., Dubale, A.A., Su, W.N., and Hwang, B.J. (2016). Using hematite for photoelectrochemical water splitting: a review of current progress and challenges. *Nanoscale Horiz.* 1, 243–267. <https://doi.org/10.1039/C5NH00098J>.
2. Kausar, A. (2020). Polymeric materials filled with hematite nanoparticle: current state and prospective application. *Polymer-Plastics Technology and Materials* 59, 323–338. <https://doi.org/10.1080/25740881.2019.1647238>.
3. Sangaiya, P., and Jayaprakash, R. (2018). A review on iron oxide nanoparticles and their biomedical applications. *J. Supercond. Nov. Magnetism* 31, 3397–3413. <https://doi.org/10.1007/s10948-018-4841-2>.
4. Barroso, M., Pendlebury, S.R., Cowan, A.J., and Durrant, J.R. (2013). Charge carrier trapping, recombination and transfer in hematite ( $\alpha$ -Fe<sub>2</sub>O<sub>3</sub>) water splitting photoanodes. *Chem. Sci.* 4, 2724–2734. <https://doi.org/10.1039/C3SC50496D>.
5. Huda, M.N., Walsh, A., Yan, Y., Wei, S.-H., and Al-Jassim, M.M. (2010). Electronic, structural, and magnetic effects of 3d transition metals in hematite. *J. Appl. Phys.* 107, 123712. <https://doi.org/10.1063/1.3432736>.
6. Zimmermann, R., Steiner, P., Claessen, R., Reinert, F., Hüfner, S., Blaha, P., and Dufek, P. (1999). Electronic structure of 3d-transition-metal oxides: on-site Coulomb repulsion versus covalency. *J. Phys. Condens. Matter* 11, 1657–1682. <https://doi.org/10.1088/0953-8984/11/7/002>.
7. Rollmann, G., Rohrbach, A., Entel, P., and Hafner, J. (2004). First-principles calculation of the structure and magnetic phases of hematite. *Phys. Rev. B* 69, 165107. <https://doi.org/10.1103/PhysRevB.69.165107>.
8. Pozun, Z.D., and Henkelman, G. (2011). Hybrid density functional theory band structure engineering in hematite. *J. Chem. Phys.* 134, 224706. <https://doi.org/10.1063/1.3598947>.
9. Liao, P., and Carter, E.A. (2010). Ab initio DFT + U predictions of tensile properties of iron oxides. *J. Mater. Chem.* 20, 6703–6719. <https://doi.org/10.1039/C0JM01199A>.
10. Coey, J.M.D., and Sawatzky, G.A. (1971). A study of hyperfine interactions in the system (Fe<sub>1-x</sub>Rh<sub>x</sub>)<sub>2</sub>O<sub>3</sub> using the Mossbauer effect (Bonding parameters). *J. Phys. C Solid State Phys.* 4, 2386–2407. <https://doi.org/10.1088/0022-3719/4/15/025>.
11. Finger, L.W., and Hazen, R.M. (1980). Crystal structure and isothermal compression of Fe<sub>2</sub>O<sub>3</sub>, Cr<sub>2</sub>O<sub>3</sub>, and V<sub>2</sub>O<sub>5</sub> to 50 kbars. *J. Appl. Phys.* 51, 5362–5367. <https://doi.org/10.1063/1.327451>.
12. Wilson, N.C., and Russo, S.P. (2009). Hybrid density functional theory study of the high-pressure polymorphs of  $\alpha$ -Fe<sub>2</sub>O<sub>3</sub> hematite. *Phys. Rev. B* 79, 094113. <https://doi.org/10.1103/PhysRevB.79.094113>.
13. Hohenberg, P., and Kohn, W. (1964). Inhomogeneous electron gas. *Phys. Rev.* 136, B864–B871. <https://doi.org/10.1103/PhysRev.136.B864>.
14. Becke, A.D. (2014). Perspective: fifty years of density-functional theory in chemical physics. *J. Chem. Phys.* 140, 18A301. <https://doi.org/10.1063/1.4869598>.
15. Kohn, W., and Sham, L.J. (1965). Self-consistent equations including exchange and correlation effects. *Phys. Rev.* 140, A1133–A1138. <https://doi.org/10.1103/PhysRev.140.A1133>.
16. Meng, Y., Liu, X.-W., Huo, C.-F., Guo, W.-P., Cao, D.-B., Peng, Q., Dearden, A., Gonze, X., Yang, Y., Wang, J., et al. (2016). When density functional approximations meet iron oxides. *J. Chem. Theor. Comput.* 12, 5132–5144. <https://doi.org/10.1021/acs.jctc.6b00640>.
17. Mori-Sánchez, P., Cohen, A.J., and Yang, W. (2006). Many-electron self-interaction error in approximate density functionals. *J. Chem. Phys.* 125, 201102. <https://doi.org/10.1063/1.2403848>.
18. Jiang, H., Gomez-Abal, R.I., Rinke, P., and Scheffler, M. (2010). First-principles modeling of localized d states with the GW @LDA + U approach. *Phys. Rev. B* 82, 045108. <https://doi.org/10.1103/PhysRevB.82.045108>.
19. Cramer, C.J., and Truhlar, D.G. (2009). Density functional theory for transition metals and transition metal chemistry. *Phys. Chem. Chem. Phys.* 11, 10757–10816. <https://doi.org/10.1039/B907148B>.



20. Piccinin, S. (2019). The band structure and optical absorption of hematite ( $\alpha$ -Fe<sub>2</sub>O<sub>3</sub>): a first-principles GW-BSE study. *Phys. Chem. Chem. Phys.* 21, 2957–2967. <https://doi.org/10.1039/C8CP07132B>.
21. Janesko, B.G. (2021). Replacing hybrid density functional theory: motivation and recent advances. *Chem. Soc. Rev.* 50, 8470–8495. <https://doi.org/10.1039/D0CS01074J>.
22. Anisimov, V.I., Zaanen, J., and Andersen, O.K. (1991). Band theory and mott insulators: hubbard U instead of stoner I. *Phys. Rev. B Condens. Matter* 44, 943–954. <https://doi.org/10.1103/PhysRevB.44.943>.
23. Anisimov, V.I., Poteryaev, A.I., Korotin, M.A., Anokhin, A.O., and Kotliar, G. (1997). First-principles calculations of the electronic structure and spectra of strongly correlated systems: dynamical mean-field theory. *J. Phys. Condens. Matter* 9, 7359–7367. <https://doi.org/10.1088/0953-8984/9/35/010>.
24. Dudarev, S.L., Botton, G.A., Savrasov, S.Y., Humphreys, C.J., and Sutton, A.P. (1998). Electron-energy-loss spectra and the structural stability of nickel oxide: an LSDA+U study. *Phys. Rev. B* 57, 1505–1509. <https://doi.org/10.1103/PhysRevB.57.1505>.
25. Himmetoglu, B., Floris, A., de Gironcoli, S., and Cococcioni, M. (2014). Hubbard-corrected DFT energy functionals: the LDA+U description of correlated systems. *Int. J. Quant. Chem.* 114, 14–49. <https://doi.org/10.1002/qua.24521>.
26. Campo, V.L., Jr., and Cococcioni, M. (2010). Extended DFT +U+V method with on-site and inter-site electronic interactions. *J. Phys. Condens. Matter* 22, 055602. <https://doi.org/10.1088/0953-8984/22/5/055602>.
27. Ricca, C., Timrov, I., Cococcioni, M., Marzari, N., and Aschauer, U. (2020). Self-consistent DFT + U + V study of oxygen vacancies in SrTiO<sub>3</sub>. *Phys. Rev. Res.* 2, 023313. <https://doi.org/10.1103/PhysRevResearch.2.023313>.
28. Timrov, I., Marzari, N., and Cococcioni, M. (2022). HP – a code for the calculation of Hubbard parameters using density-functional perturbation theory. *Comput. Phys. Commun.* 279, 108455. <https://doi.org/10.1016/j.cpc.2022.108455>.
29. Timrov, I., Marzari, N., and Cococcioni, M. (2018). Hubbard parameters from density-functional perturbation theory. *Phys. Rev. B* 98, 085127. <https://doi.org/10.1103/PhysRevB.98.085127>.
30. Kirchner-Hall, N.E., Zhao, W., Xiong, Y., Timrov, I., and Dabo, I. (2021). Extensive benchmarking of DFT+U calculations for predicting band gaps. *Appl. Sci.* 11, 2395. <https://doi.org/10.3390/app11052395>.
31. Timrov, I., Marzari, N., and Cococcioni, M. (2021). Self-consistent Hubbard parameters from density-functional perturbation theory in the ultrasoft and projector-augmented wave formulations. *Phys. Rev. B* 103, 045141. <https://doi.org/10.1103/PhysRevB.103.045141>.
32. Mahajan, R., Timrov, I., Marzari, N., and Kashyap, A. (2021). Importance of intersite Hubbard interactions in  $\beta$ -MnO<sub>2</sub>: a first-principles DFT + U + V study. *Phys. Rev. Mater.* 5, 104402. <https://doi.org/10.1103/PhysRevMaterials.5.104402>.
33. Kulik, H.J., and Marzari, N. (2011). Accurate potential energy surfaces with a DFT+U(R) approach. *J. Chem. Phys.* 135, 194105. <https://doi.org/10.1063/1.3660353>.
34. Rohrbach, A., Hafner, J., and Kresse, G. (2004). Ab initio study of the (0001) surfaces of hematite and chromia: influence of strong electronic correlations. *Phys. Rev. B* 70, 125426. <https://doi.org/10.1103/PhysRevB.70.125426>.
35. Rollmann, G., Entel, P., Rohrbach, A., and Hafner, J. (2005). High-pressure characteristics of  $\alpha$ -Fe<sub>2</sub>O<sub>3</sub> using DFT+U. *Phase Transitions* 78, 251–258. <https://doi.org/10.1080/01411590412331316546>.
36. Adelstein, N., Neaton, J.B., Asta, M., and De Jonghe, L.C. (2014). Density functional theory based calculation of small-polaron mobility in hematite. *Phys. Rev. B* 89, 245115. <https://doi.org/10.1103/PhysRevB.89.245115>.
37. Bassi, P.S., Gurudayal, Wong, L.H., and Barber, J. (2014). Iron based photoanodes for solar fuel production. *Phys. Chem. Chem. Phys.* 16, 11834–11842. <https://doi.org/10.1039/C3CP55174A>.
38. Dzade, N., Roldan, A., and de Leeuw, N. (2014). A density functional theory study of the adsorption of benzene on hematite ( $\alpha$ -Fe<sub>2</sub>O<sub>3</sub>) surfaces. *Minerals* 4, 89–115. <https://doi.org/10.3390/min4010089>.
39. Guo, Y., Clark, S.J., and Robertson, J. (2012). Electronic and magnetic properties of Ti<sub>2</sub>O<sub>3</sub>, Cr<sub>2</sub>O<sub>3</sub>, and Fe<sub>2</sub>O<sub>3</sub> calculated by the screened exchange hybrid density functional. *J. Phys. Condens. Matter* 24, 325504. <https://doi.org/10.1088/0953-8984/24/32/325504>.
40. Pauling, L., and Hendricks, S.B. (1925). The crystal structures of hematite and corundum. *J. Am. Chem. Soc.* 47, 781–790. <https://doi.org/10.1021/ja01680a027>.
41. Bødker, F., Hansen, M.F., Koch, C.B., Lefmann, K., and Mørup, S. (2000). Magnetic properties of hematite nanoparticles. *Phys. Rev. B* 61, 6826–6838. <https://doi.org/10.1103/PhysRevB.61.6826>.
42. Huang, X., Ramadugu, S.K., and Mason, S.E. (2016). Surface-specific DFT + U approach applied to  $\alpha$ -Fe<sub>2</sub>O<sub>3</sub>(0001). *J. Phys. Chem. C* 120, 4919–4930. <https://doi.org/10.1021/acs.jpcc.5b12144>.
43. Hill, A.H., Jiao, F., Bruce, P.G., Harrison, A., Kockelmann, W., and Ritter, C. (2008). Neutron diffraction study of mesoporous and bulk hematite,  $\alpha$ -Fe<sub>2</sub>O<sub>3</sub>. *Chem. Mater.* 20, 4891–4899. <https://doi.org/10.1021/cm800009s>.
44. Fujimori, A., Saeki, M., Kimizuka, N., Taniguchi, M., and Suga, S. (1986). Photoemission satellites and electronic structure of Fe<sub>2</sub>O<sub>3</sub>. *Phys. Rev. B Condens. Matter* 34, 7318–7328. <https://doi.org/10.1103/PhysRevB.34.7318>.
45. Kurtz, R.L., and Henrich, V.E. (1987). Surface electronic structure and chemisorption on corundum transition-metal oxides:  $\alpha$ -Fe<sub>2</sub>O<sub>3</sub>. *Phys. Rev. B Condens. Matter* 36, 3413–3421. <https://doi.org/10.1103/PhysRevB.36.3413>.
46. Ma, Y., Johnson, P.D., Wassdahl, N., Guo, J., Skytt, P., Nordgren, J., Kevan, S.D., Rubensson, J., Böske, T., and Eberhardt, W. (1993). Electronic structures of  $\alpha$ -Fe<sub>2</sub>O<sub>3</sub> and Fe<sub>3</sub>O<sub>4</sub> from O K-edge absorption and emission spectroscopy. *Phys. Rev. B Condens. Matter* 48, 2109–2111. <https://doi.org/10.1103/PhysRevB.48.2109>.
47. Fdez-Gubieda, M.L., García-Prieto, A., Alonso, J., and Meneghini, C. (2016). X-ray absorption fine structure spectroscopy in Fe oxides and oxyhydroxides. *Iron Oxides* 397–422, 397–422. <https://doi.org/10.1002/9783527691395.ch17>.
48. Corrias, A., Ennas, G., Mountjoy, G., and Paschina, G. (2000). An X-ray absorption spectroscopy study of the Fe K edge in nanosized maghemite and in Fe<sub>2</sub>O<sub>3</sub>-SiO<sub>2</sub> nanocomposites. *Phys. Chem. Chem. Phys.* 2, 1045–1050. <https://doi.org/10.1039/A908698F>.
49. O'day, P.A., Rivera, N., Root, R., and Carroll, S.A. (2004). X-ray absorption spectroscopic study of Fe reference compounds for the analysis of natural sediments. *Am. Mineral.* 89, 572–585. <https://doi.org/10.2138/am-2004-0412>.
50. Pascarella, S. (2015). In *Studies of Matter at Extreme Conditions BT - Synchrotron Radiation: Basics, Methods and Applications*, S. Mobilio, F. Boscherini, and C. Meneghini, eds. (Springer Berlin Heidelberg), pp. 737–760. [https://doi.org/10.1007/978-3-642-55315-8\\_29](https://doi.org/10.1007/978-3-642-55315-8_29).
51. Henderson, G.S., de Groot, F.M.F., and Moulton, B.J.A. (2014). X-Ray absorption near-edge structure (XANES) spectroscopy. *Rev. Mineral. Geochem.* 78, 75–138. <https://doi.org/10.2138/rmg.2014.78.3>.
52. Wilke, M., Farges, F., Petit, P.-E., Brown, G.E., Jr., and Martin, F. (2001). Oxidation state and coordination of Fe in minerals: an Fe K-XANES spectroscopic study. *Am. Mineral.* 86, 714–730. <https://doi.org/10.2138/am-2001-5-612>.
53. Wu, Z.Y., Gota, S., Jollet, F., Pollak, M., Gautier-Soyer, M., and Natoli, C.R. (1997). Characterization of iron oxides by x-ray absorption at the oxygen K edge using a full multiple-scattering approach. *Phys. Rev. B* 55, 2570–2577. <https://doi.org/10.1103/PhysRevB.55.2570>.
54. Mitterbauer, C., Kothleitner, G., Grogger, W., Zandbergen, H., Freitag, B., Tiemeijer, P., and Hofer, F. (2003). Electron energy-loss near-edge structures of 3d transition metal oxides recorded at high-energy resolution. *Ultramicroscopy* 96, 469–480. [https://doi.org/10.1016/S0304-3991\(03\)00109-8](https://doi.org/10.1016/S0304-3991(03)00109-8).
55. Giannozzi, P., Baroni, S., Bonini, N., Calandra, M., Car, R., Cavazzoni, C., Ceresoli, D.,



- Chiarotti, G.L., Cococcioni, M., Dabo, I., et al. (2009). Quantum ESPRESSO: a modular and open-source software project for quantum simulations of materials. *J. Phys. Condens. Matter* 21, 395502. <https://doi.org/10.1088/0953-8984/21/39/395502>.
56. Prandini, G., Marrazzo, A., Castelli, I.E., Mounet, N., and Marzari, N. (2018). Precision and efficiency in solid-state pseudopotential calculations. *npj Comput. Mater.* 4, 72. <https://doi.org/10.1038/s41524-018-0127-2>.
57. Cococcioni, M., and de Gironcoli, S. (2005). Linear response approach to the calculation of the effective interaction parameters in the LDA+U method. *Phys. Rev. B* 71, 035105. <https://doi.org/10.1103/PhysRevB.71.035105>.
58. Momma, K., and Izumi, F. (2011). VESTA 3 for three-dimensional visualization of crystal, volumetric and morphology data. *J. Appl. Crystallogr.* 44, 1272–1276. <https://doi.org/10.1107/S0021889811038970>.
59. Marzari, N., Vanderbilt, D., De Vita, A., and Payne, M.C. (1999). Thermal contraction and disordering of the Al(110) surface. *Phys. Rev. Lett.* 82, 3296–3299. <https://doi.org/10.1103/PhysRevLett.82.3296>.
60. Taillefumier, M., Cabaret, D., Flank, A.-M., and Mauri, F. (2002). X-ray absorption near-edge structure calculations with the pseudopotentials: application to the K edge in diamond and  $\alpha$ -quartz. *Phys. Rev. B* 66, 195107. <https://doi.org/10.1103/PhysRevB.66.195107>.
61. Gougousis, C., Calandra, M., Seitsonen, A., Brouder, C., Shukla, A., and Mauri, F. (2009). Intrinsic charge transfer gap in NiO from Ni K-edge x-ray absorption spectroscopy. *Phys. Rev. B* 79, 045118. <https://doi.org/10.1103/PhysRevB.79.045118>.
62. Timrov, I., Agrawal, P., Zhang, X., Erat, S., Liu, R., Braun, A., Cococcioni, M., Calandra, M., Marzari, N., and Passerone, D. (2020). Electronic structure of pristine and Ni-substituted LaFeO<sub>3</sub> from near edge x-ray absorption fine structure experiments and first-principles simulations. *Phys. Rev. Res.* 2, 033265. <https://doi.org/10.1103/PhysRevResearch.2.033265>.
63. Bunău, O., and Calandra, M. (2013). Projector augmented wave calculation of x-ray absorption spectra at the L<sub>2,3</sub> edges. *Phys. Rev. B* 87, 205105. <https://doi.org/10.1103/PhysRevB.87.205105>.
64. Paris, E., Simonelli, L., Wakita, T., Marini, C., Lee, J.-H., Olszewski, W., Terashima, K., Kakuto, T., Nishimoto, N., Kimura, T., et al. (2016). Temperature dependent local atomic displacements in ammonia intercalated iron selenide superconductor. *Sci. Rep.* 6, 27646. <https://doi.org/10.1038/srep27646>.
65. Rehr, J.J., and Albers, R.C. (2000). Theoretical approaches to x-ray absorption fine structure. *Rev. Mod. Phys.* 72, 621–654. <https://doi.org/10.1103/RevModPhys.72.621>.
66. Ravel, B., and Newville, M. (2005). Data analysis for X-ray absorption spectroscopy using IFEFFIT. *J. Synchrotron Radiat.* 12, 537–541. <https://doi.org/10.1107/S0909049505012719>.
67. Williams, T., Kelley, C., and Crawford, D. (2017). *Gnuplot 5.2 Manual: An Interactive Plotting Program* (12th Media Services).

## STAR★METHODS

### KEY RESOURCES TABLE

REAGENT or RESOURCE	SOURCE	IDENTIFIER
Software and Algorithms		
Quantum ESPRESSO	Quantum ESPRESSO Foundation.	<a href="https://www.quantum-espresso.org/">https://www.quantum-espresso.org/</a>
VESTA software package	JP-Minerals	<a href="https://jp-minerals.org/vesta/en/">https://jp-minerals.org/vesta/en/</a>
Gnuplot	Gnuplot	<a href="http://www.gnuplot.info/">http://www.gnuplot.info/</a>
SSSP Precision Library v1.2	Materials Cloud	<a href="https://www.materialscloud.org/discover/sssp/table/precision">https://www.materialscloud.org/discover/sssp/table/precision</a>
ATHENA/ARTEMIS	DEMETER	<a href="https://bruceravel.github.io/demeter/">https://bruceravel.github.io/demeter/</a>
$\alpha$ -Fe <sub>2</sub> O <sub>3</sub> CIF entry # 9015964	Crystallography Open Database (COD)	<a href="http://www.crystallography.net/cod/">http://www.crystallography.net/cod/</a>

### RESOURCE AVAILABILITY

#### Lead contact

Further information and requests for resources should be directed to the lead contact, Nelson Naveas ([nelson.naveas@estudiante.uam.es](mailto:nelson.naveas@estudiante.uam.es)).

#### Materials availability

This study did not generate new unique reagents.

#### Data and code availability

All data reported in this paper will be shared by the [lead contact](#) upon request. This paper does not report original code.

### EXPERIMENTAL MODEL AND SUBJECT DETAILS

Our study does not use experimental models typical in the life sciences.

### METHOD DETAILS

DFT calculations were carried out using the plane-wave (PW) pseudopotential approach implemented in the Quantum ESPRESSO computational package.<sup>55</sup> PBEsol Pseudopotentials were obtained from the SSSP Precision Library v1.2.<sup>56</sup> We investigated different magnetic configurations based on the orientation of the local spin density around the Fe atoms of the structures depicted in [Figure 1](#). These magnetic configurations were denoted as AFM-1 (++ -), AFM-2 (+- +) and AFM-3 (+- -) for the antiferromagnetic spin ordering, as well as FM (++ +) for the ferromagnetic spin ordering. The rhombohedral primitive and the conventional unit cell comprising 10 and 30 atoms, respectively, were used.

The crystal structures were optimized using the BFGS quasi-newton algorithm by DFT, DFT + U, and DFT + U + V methods. We specified a convergence threshold of  $1 \times 10^{-6}$  Ry for total energy,  $1 \times 10^{-5}$  Ry/Bohr for forces, and 0.5 kbar for pressure. On one side, DFT + U calculations were carried out using the simplified rotational-invariant formulation adopted by Cococcioni and de Gironcoli<sup>57</sup> by using a Hubbard U correction on Fe-3d states. On the other side, DFT + U + V calculations were performed using the simplified version of Campo Jr and Cococcioni<sup>26</sup> by correcting the inter-site interaction between the Fe-3d and O-2p states using the Hubbard V parameter. The Hubbard parameters were calculated using the HP code by DFPT and using uniform  $\Gamma$ -centered k and q point meshes.<sup>29</sup> At this stage, we used the primitive cells with a  $4 \times 4 \times 4$  k points mesh and the  $2 \times 2 \times 2$  q points mesh. In DFPT calculations, we used a kinetic-energy cutoff of 65 Ry for the wave function and 780 Ry for the charge density (detailed information about the SCF and HP calculation input files can be seen in the [Data S1](#) and [Data S2](#), respectively, of the Supplemental Data file). All parameters used in our calculations were previously evaluated and chosen according to their proper convergence tests. We employed the self-consistent technique to calculate U and V, which entails cycling calculations, including structural optimizations and Hubbard parameters

re-computing for each new optimized crystal geometry.<sup>31</sup> The crystal structures were visualized using the VESTA software package.<sup>58</sup>

For the DFT + U and DFT + U + V calculations, two different types of Hubbard projectors, non-orthogonalized atomic orbitals (NAO) and orthogonalized atomic orbitals (OAO) were utilized.<sup>31</sup> We employed the Marzari-Vanderbilt (MV) smearing method<sup>59</sup> with a broadening parameter of  $1 \times 10^{-3}$  Ry.

Structural optimizations, magnetic moments, band gaps, and the projected and total density of states (DOS) were made using a uniform  $\Gamma$ -centered k points mesh of size  $8 \times 8 \times 8$ . We used a kinetic-energy cut-off of 90 Ry for the wave function and 1080 Ry for the charge density.

Experimental X-ray absorption spectroscopy (XAS) measurements were performed at room temperature under vacuum conditions. The K-edge of Fe ( $\sim 7124$  eV) was performed in continuous mode at the CLÆSS beamline of the ALBA CELLS synchrotron (Spain) using a double-crystal Si (311) monochromator. Energy calibration has been checked for each collected spectrum by aligning the first derivative maximum (7112 eV) of the XAS reference spectrum of a Fe foil, acquired simultaneously with the sample. The absorption data were collected in transmission mode using three ionization chambers properly gas-filled at this energy. In the XANES region, all the spectra have been sampled with an energy resolution of 0.3 eV. The spectra have been treated according to the standard procedure: pre-edge background subtraction and XANES normalization were carried out by fitting a linear polynomial to the pre-edge region and a cubic polynomial to the post-edge region of the absorption spectrum. Spectra have been divided by absorption jump. The data processing was performed using the software ATHENA, part of the package IFEFFIT.

Simulations of Fe and O K-edge XANES spectra were conducted by computing the dipole part using the Lanczos recursive procedure inside the XSpectra code of Quantum Espresso Distribution.<sup>60–62</sup> We approached the calculations by ignoring both the quadrupole part and the core-hole in the final state. The convolution of the XANES spectra was made using a Lorentzian smearing arctangentlike function with an energy-dependent broadening.<sup>63</sup>

The EXAFS signal of  $\alpha$ -Fe<sub>2</sub>O<sub>3</sub> has been extracted by subtracting a smooth post-edge background function. Corresponding Fourier Transforms have been performed over the k range 2.6–14 Å<sup>−1</sup> after being multiplied by k<sup>2</sup> to enhance the signal in the higher k-region.<sup>64</sup> EXAFS oscillations have been modeled by using the structures obtained after relaxation within the different ab-initio approximations. Theoretical amplitudes and phases of the different paths used in the analysis have been calculated by the FEFF-6 code<sup>65</sup> and then adjusted to the experimental data (in R space) using the ARTEMIS program of the DEMETER suite.<sup>66</sup> All plots were generated using GNUpot V5.2 program.<sup>67</sup>

## QUANTIFICATION AND STATISTICAL ANALYSIS

In the experimental XAS measurements, several scans were collected to ensure reproducibility and improve the signal-to-noise ratio. The raw data has been treated by pre-edge background subtraction, and XANES normalization was carried out by fitting a linear polynomial to the pre-edge region and a cubic polynomial to the post-edge region of the absorption spectrum. The EXAFS signal has been extracted and modeled by the standard theory equations. The normalized sum of square residuals was used as a measure of the discrepancy between the unknown data and the fit model.

## ADDITIONAL RESOURCES

We have no relevant additional resources.